Bulletin of the Seismological Society of America, Vol. 99, No. 3, pp. 1827–1840, June 2009, doi: 10.1785/0120080234

A Method for Rapid Determination of Moment Magnitude M_w for Moderate to Large Earthquakes from the Near-Field Spectra of Strong-Motion Records (MWSYNTH)

by Bertrand Delouis, Jean Charlety, and Martin Vallée

Abstract Seismic moment and the corresponding moment magnitude M_w are classically obtained from the spectrum of far-field body waves. Near-field records are generally not used for that purpose, particularly in the case of large earthquakes because different types of wave arrive simultaneously, preventing the definition of a simple relation between the seismic moment and the spectrum. We developed an original method to determine M_w from the displacement spectra of near-field records. The spectral amplitude at low frequency obtained from the real records is compared to that of synthetic records computed using kinematic rupture models scaled with M_w. Synthetic records are computed and averaged for various fault orientations and for epicentral distances ranging from 1 to 100 km. The initial portion of the spectrum affected by baseline shift in the acceleration records is automatically identified and removed by high-pass filtering using a cutoff frequency adapted to each station. The synthetic spectral values as a function of moment magnitude, epicentral distance, and filtering are computed only once and stored in tables. The spectral amplitudes of the real records are simply interpolated in the tables of synthetic data, allowing a fast determination of M_w. The method has been validated using 22 shallow earthquakes (depth < 50 km) with magnitude ranging from 3.9 to 7.7. We show that a window of 80 sec of signal after the earthquake origin time provides robust values of M_w for the whole magnitude range considered here. Shorter time windows may be used but with M_w underestimated for large events. The method is well suited for near real-time fast determination of M_w.

Introduction

Being a logarithmic representation of the seismic moment, the moment magnitude M_w (Kanamori, 1977) is the magnitude that best characterizes the earthquake size, although some earthquake properties may be better described by other magnitudes such as the energy magnitude M_e for the shaking strength. It is classically obtained from the far-field displacement spectrum of body waves (*P* or *S*), at a distance where the source can be approximated by a point source. In such condition the seismic moment can be analytically related to the spectral amplitude (Brune, 1970, 1971). Seismic moment is also routinely determined by centroid moment tensor inversions based on regional or teleseismic waveform modeling (e.g., Mediterranean Very Broadband Seismic Network [MEDNET], Swiss Seismological Service, Swiss Federal Institute of Technology in Zurich, Switzerland [SED/ETHZ], Global Centroid Moment Tensor catalog [GCMT], National Research Institute for Earth Science and Disaster Prevention [NIED]; see Data and Resources section).

Near-field seismograms obtained from near-source accelerometers represent the earliest available data for rapid seismic alert. Several studies have addressed the possibility of obtaining the magnitude from the initial part of the *P* wave, allowing seismic early warning before damaging ground motion occurs. These studies have revealed linear relations between the magnitude and some properties of the first few seconds of the *P* wave, such as the dominant period (Allen and Kanamori, 2003; Wu and Kanamori, 2008) or the peak ground displacement in a certain frequency range (Wu and Zhao, 2006; Zollo *et al.*, 2006). In those relations a large scatter of the early *P*-wave parameter is observed, but this scatter can be substantially reduced by averaging data from several stations. These results suggest that the rupture is to some degree deterministic; that is, that some characteristics of the first few seconds of rupture scale with the final magnitude of the earthquake. In our approach we obtain the magnitude from the seismic moment by comparing the spectral characteristics of observed and synthetic seismograms.

Our fundamental aim is to obtain a robust estimate of moment magnitude M_w within a time scale of one to two minutes after earthquake origin time. Nonetheless, we will address the possibility of obtaining M_w with time windows as short as 5, 10, or 20 sec after rupture onset.

The relation between the spectrum of near-field seismograms and the seismic moment, especially in the case of large earthquakes, is not straightforward. Near-source seismograms result from complex interferences of far-, intermediate-, and near-field waves influenced by the finite dimension character of the rupture process. The resulting intermixed waves combine different radiation patterns and geometrical expansion factors ($1/r$ for far field and $1/r^2$ for near and intermediate field, Aki and Richards, 1980; Wu and Ben-Mehahem, 1985), as well as different wave velocities (P and S), preventing the definition of a simple analytical relation between the spectrum and the seismic moment. It can be difficult, even impossible, to identify and individualize the far-field P and S waves at short distance from a large earthquake. This is illustrated by Figure 1. At a distance of 24 km, the displacement seismogram of a moderate size event (M_w 4.6 Nice earthquake in France, Fig. 1a) exhibits clear P and S phases. At a distance of 48 km, the displacement record of a large event (M_w 7.2 Düzce earthquake in Turkey, Fig. 1b) displays a totally different character. The diverse kinds of waves emitted by the rupture are intermixed, with a much stronger influence of near- and intermediate-field waves, giving rise to an overall long period signal where the P and S waves cannot be distinguished. In such a case moment magnitude could be obtained by modeling the seismogram using a slip inversion procedure (e.g., Delouis *et al.*, 2009). However, computing time would become a concern and an estimate of moment magnitude is generally required to set up model parameters before slip inversion.

We present an original approach, hereafter called MWSYNTH, in which observed displacement spectra are compared with synthetic spectra computed for a variety of finite dimension source models in the near-field domain. Before any earthquake is analyzed, we generate synthetic seismograms for a series of hypothetical finite dimension sources. The synthetic seismograms include effects of source finiteness as well as the complete displacement field (near, intermediate, and far field) generated in a simple 1D layered velocity model. Each source model is sized according to a specific seismic moment, hence to moment magnitude. The set of synthetic seismograms is representative of a wide range of possible scenarios. Then the synthetic displacement spectra are computed, and the values of the spectral levels are stored in tables. We show that the spectral plateau at low frequency, hereafter called the spectral level, scales with moment magnitude. To determine the moment magnitude of a specific earthquake the displacement spectra of the real records are computed, the spectral levels retrieved, and the moment magnitude obtained from the corresponding synthetic spectral levels interpolated in the precomputed tables.

The frequency response of digital accelerographs is nominally flat in acceleration from direct current (DC), or 0 frequency to 50 Hz, but baseline offsets are usually observed during seismic shaking. These offsets in acceleration can produce unreasonable displacements after double integration and contaminate the displacement spectra at low frequency. Empirical methods may be used to correct for this effect (e.g., Iwan, 1985; Boore, 2001; Wu and Wu, 2007) but not in a fully automated way. To overcome this problem we compute spectral levels after high-pass filtering. The degree

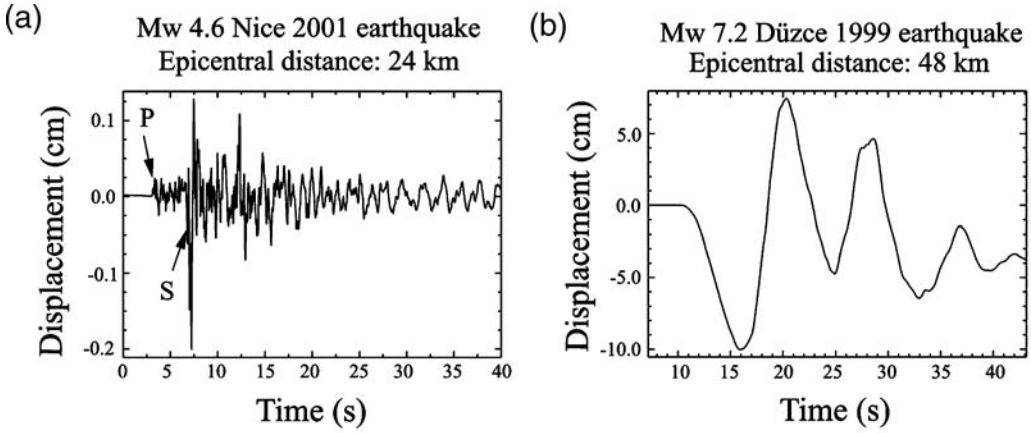

Figure 1. Waveform characteristics of near-source records for a moderate and a large earthquake. (a) Unfiltered displacement seismogram of the M_w 4.6 earthquake of Nice (France) in 2001, recorded at a distance of 24 km. Individualized far-field P- and S-wave trains can be identified. East component of station NBOR. (b) Unfiltered displacement seismogram of the M_w 7.2 earthquake of Düzce (Turkey) in 1999, recorded at a distance of 48 km. Individualized P- and S-wave trains cannot be identified. East component of station IRIGM 362. In part (a) the station is located at a distance much larger than the rupture dimension, and far-field waves dominate (P, S, and associated codas). In part (b) epicentral distance is of the same order as rupture dimension, and the signal exhibits a long-period character resulting from the intermixing of all wave types (far-, intermediate, and near-field waves) generated during the rupture process. Windowing around the P or S wave in order to compute the far-field displacement spectrum is possible for part (a) but not for part (b).

of filtering should be chosen appropriately to eliminate the baseline effect without removing too much of the low-frequency waves characterizing large earthquakes. This is done by analyzing the shape of the acceleration spectrum at low frequency.

To assess the possibility of obtaining early estimates of the moment magnitude, and to analyze how the length of the time window influences the value of the computed magnitude, spectra are calculated for different time windows. Precomputing of synthetic seismograms and construction of tables with spectral level are performed only once. The processing of real records and determination of M_w by interpolation in the tables of synthetic values could be implemented as a real-time automated procedure. In this study we test the method offline for a number of recent earthquakes worldwide (Table 1) with magnitude ranging from 3.9 to 7.7. We consider only earthquakes occurring at shallow depth (<50 km) and with epicentral distances less than 100 km. However, the approach could be extended for deeper events and larger distances.

The MWSYNTH Method

Synthetic Seismograms and Tables of Spectral Levels

Our goal is to determine the moment magnitude of earthquakes very soon after occurrence, before any source or focal mechanism inversions have been performed. The only prerequisites are the hypocentral location and the detection of the first P arrival at each station. Focal mechanism influences the displacement spectrum via the radiation pattern. Using a specific focal mechanism to produce synthetic seismograms could lead to strong biases if this mechanism is far from the real one. To overcome this difficulty we average the effects of various focal mechanisms. Synthetic seismograms are generated for six different focal mechanisms (strike/dip/rake $= 0/90/0$, $90/90/0$, $0/45/90$, $90/45/90$, $45/45/90$, and $135/45/90$), corresponding to dip-slip and strike-slip faulting, for a station located 1–100 km from the epicenter in the single azimuth N70°E arbitrarily chosen (Fig. 2a). It should be noted that from the spectral point of view, the sense of fault motion is indifferent. A change from reverse to normal or from left-lateral to right-lateral does not affect the spectral level.

The source is represented by a simple kinematic model. Rupture area and slip are scaled with moment magnitude. The hypocenter, where rupture initiates, is located at 15 km depth. The rupture plane is square for small to moderate earthquakes whose rupture does not reach the surface, and rectangular, more stretched along strike than along dip, for larger ones (Fig. 2b). Rupture area is derived from the regression relations of Wells and Coppersmith (1994). The dislocation (slip), assumed constant on the fault, is determined from the relation $\Delta u = M_0/(\mu.1.w)$ where μ is rigidity and l, w are rupture length and width, respectively. M_0 is obtained from M_w using the formula of Kanamori (1977): $M_w = (2/3)\log(M_0) - 6.06$, with M_0 in N m. The continuous rupture is represented by a discrete sum of point sources evenly distributed on the fault plane. For each point source the local source time function is a triangular function whose rise time is fixed assuming a slip velocity of 1 m/sec. From the center of the fault, which coincides with the hypocenter, rupture propagates symmetrically in all directions until it reaches the borders of the rupture plane (Fig. 2b). Rupture velocity is fixed to 2.7 km/sec. The complete displacement field generated by the source is computed using the discrete wavenumber method of Bouchon (1981) for a 1D layered velocity model (Table 2). The number of point sources used to simulate the fault rupture depends on M_w from 5×5 (M_w 2) to 81×15 (M_w 8). Seismograms for M_w ranging from 2 to 8 are computed and stored for later use.

The spectra of synthetic displacement seismograms are computed for different window lengths and high-pass frequencies. We define nine signal windows, ending 5, 10, 20, 30, 40, 50, 60, 70, and 80 sec after earthquake origin time, and 25 high-pass frequencies varying from 0.005 to 0.8 Hz. In total, 225 tables are computed once and stored for later use. We define the spectral level as the maximum value of the displacement spectra at low frequency, corresponding to the spectral plateau. Figure 3 illustrates the scaling of spectral level with moment magnitude for unfiltered (Fig. 3b) and filtered (Fig. 3c) synthetic seismograms. The values stored in the tables are the spectral levels averaged over the three components (north–south, east–west, and vertical) of the seismograms and over the six different focal mechanisms. Figure 4 displays a graphical representation of such tables for unfiltered and high-pass filtered (0.05 Hz) synthetic data. For a given magnitude the spectral level decreases with distance, as expected from geometric wave attenuation. High-pass filtering preserves the possibility of discriminating among the different magnitude values, though with less accuracy for large magnitude events as indicated by the reduced distance between the M_w 7 and M_w 8 curves in the filtered diagram (Fig. 4b).

Processing of Strong-Motion Records

Initial processing of real seismograms includes computing the average amplitude of the preevent noise (3 sec preceding the first P arrival), subtracting it from the whole signal, and cutting the record at the end of the selected time window. It may happen that reverberating waves generated in the shallow crustal layers dominate in the late section of the displacement records, beyond the direct contribution of the source. Those late arrivals can affect the displacement spectrum at low frequency, resulting in an overestimation of the magnitude. To limit this effect we perform a test on the acceleration level in a similar way as in Wu and Teng (2004). If acceleration decreases to less than 20% of the overall maximum acceleration and remains below that threshold during five contiguous seconds, the source contribution is assumed to be completed and the following part of the signal is set to amplitude zero.

Table 1
Earthquake Data

Event Number	Name	Date (dd/mm/yy), Time (UTC)	Latitude	Longitude	Depth (km)	Reference for Location*	M_w	Reference for M_w*	M_w from This Study	Source of Data
1	Tocopilla	14/11/07, 15:41	−22.33	−70.16	45	2	7.7, 7.7	1, 2	7.66	RAGIC
2	Chi-Chi	20/09/99, 17:47	23.85	120.82	8	3	7.6, 7.6, 7.6	1, 4, 5	7.67	CWB
3	Izmit	17/08/99, 00:01	40.76	29.97	11	6, 7	7.6, 7.5, 7.4, 7.6	1, 8, 9, 7	7.62	COSMOS
4	Miyagi-Oki	16/08/05, 02:46	38.15	142.28	42	14	7.2	1	7.11	K-NET
5	Duzce	12/11/99, 16:57	40.82	31.20	12	10	7.1, 7.1, 7.15, 7.2	1, 11, 12, 13	7.19	ESD
6	Pingtung Number 1	26/12/06, 12:26	21.67	121.56	44	15	7.0	1	7.07	CWB
7	Pingtung Number 2	26/12/06, 12:34	21.97	121.42	36	15	6.9	1	6.99	CWB
8	Boumerdes	21/05/03, 18:44	36.83	3.65	6	1, 16	6.8, 6.9	16	6.94	CGS
9	Chengkung	10/12/03, 04:38	23.07	121.40	18	15	6.8, 6.8, 6.8	1, 17, 18	6.87	CWB
10	Tottori	06/10/00, 04:30	35.27	133.35	12	19	6.7, 6.8, 6.7	1, 20, 21	6.73	K-NET
11	Lesser Antilles Number 1 (Saintes, France)	21/11/04, 11:41	15.76	−61.53	14	24	6.3	1	6.38	RAP
12	Taitung	01/04/06, 10:02	22.89	121.08	11	22	6.1, 6.1	1, 22	6.32	CWB
13	Parkfield	28/09/04, 17:15	35.82	−120.37	8	23	6.0, 6.0	23, 1	6.22	COSMOS
14	Lesser Antilles Number 2 (Saintes, France)	14/02/05, 18:05	15.80	−61.58	13	24	5.8	1	6.16	RAP
15	Anza	12/06/05, 15:41	33.53	−116.58	14	25	5.2, 5.2	25, 1	5.30	COSMOS
16	Lesser Antilles Number 3 (Offshore Martinique, France)	30/08/05, 14:02	15.01	−60.47	49	24	4.9	1	4.79	RAP
17	Rambervillers Northeast France	22/02/03, 20:41	48.32	6.67	11	26	4.8, 4.8	27, 28	4.74	RAP
18	Argeles-Gazost French Pyrenees	17/11/06, 18:19	43.03	0.01	9	29	4.5	32	4.51	RAP
19	Roulans-Besançon, East France	23/02/04, 17:31	47.30	6.28	15	30, 31	4.5	27	4.49	RAP
20	Vallorcine, East France	08/09/05, 11:27	46.03	6.88	7.0	27	4.5, 4.4, 4.6	27, 28, 1	4.47	RAP
21	Nice, France	25/02/01, 18:34	43.534	7.501	12	31	4.5, 4.5	27, 28	4.74	RAP
22	Aucun-Estaing, Southwest France	16/05/02, 14:56	42.93	-0.14	10	29	3.9	27	4.05	RAP

*References for location and M_w: (1) CGMT; (2) Delouis *et al.* (2009); (3) Chang *et al.* (2000); (4) Ji *et al.* (2003); (5) Ma *et al.* (2001); (6) Kandilli Observatory, Turkey; (7) Delouis *et al.* (2002); (8) Reilinger *et al.* (2000); (9) Yagi and Kikuchi (2000); (10) Milkereit *et al.* (2000); (11) Tibi *et al.* (2001); (12) Bürgmann *et al.* (2002); (13) Ayhan *et al.* (2001); (14) JMA and K-NET; (15) CWB; (16) Delouis *et al.* (2004); (17) Wu *et al.* (2006a); (18) Mozziconacci *et al.* (2008); (19) Ohmi (2002); (20) Iwata and Sekiguchi (2002); (21) Semmane *et al.* (2005); (22) Wu *et al.* (2006b); (23) Liu *et al.* (2006); (24) Bertil *et al.* (2005); (25) CISN; (26) BCSF; (27) SED/ETHZ; (28) MEDNET–INGV EMRCMT; (29) OMP; (30) RéNaSS; (31) IGN. For all acronyms see the Data and Resources section.

Theoretical acceleration spectra in the far field are characterized by f^2 rise at frequencies below the corner frequency, followed by a plateau (Aki and Richards, 1980). Near-field synthetic seismograms reveal a steady rise at low frequency, although not necessarily as f^2. In the absence of noise the acceleration spectra exhibit a continuous rise in the initial part followed by a plateau or decay in the midhigh frequency range. This characteristic behavior is observed for real acceleration records unaffected by baseline shifts (e.g., Fig. 5c). On the other hand, baseline shifts induce an over

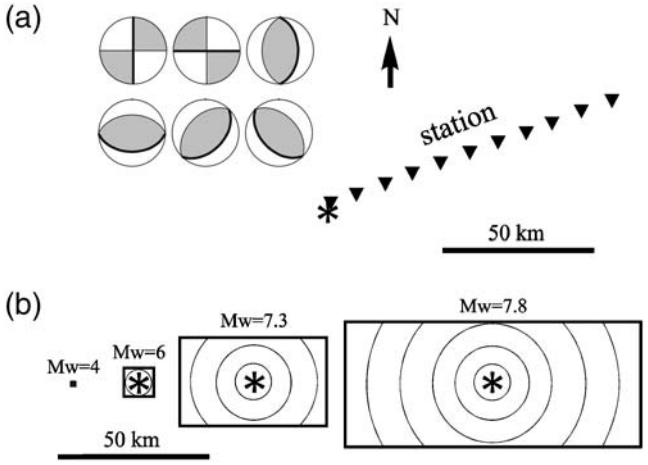

Figure 2. (a) The six different focal mechanisms (rupture plane in bold) and relative position of the seismic stations (black triangles) with respect to the hypocenter (star) used to compute the synthetic seismograms. (b) Dimensioning of the kinematic source models used >to generate the synthetic seismograms as a function of moment magnitude. The square or rectangular frames show the rupture area. Rupture initiates at the hypocenter (star) at the center of the fault model and propagates symmetrically at a constant velocity. The concentric circles represent the rupture front at different time increments.

amplification of the lowest frequencies, resulting in a strong curvature of the low-frequency part of the acceleration spectrum, which becomes *V*-shaped (e.g., Fig. 5d). The point of maximum curvature at low frequency, corresponding to the bottom of the *V* shape where the variation of the slope is at its maximum, can be used to define an effective high-pass cutoff frequency to remove the low-frequency noise. We developed an automated algorithm to detect if the low-frequency part of the acceleration spectrum is curved and to pick the frequency at which the curvature occurs. Figure 5 shows that some components, such as the east component of TCU074 for the Chi-Chi earthquake, may not need any high-pass filtering, but they represent exceptional cases. The east component of CHYO80 exhibits a more common behavior. For that component the high-pass frequency has been determined on the acceleration spectra (0.07 Hz, Fig. 5d) and the low-frequency noise can be effectively removed (Fig. 5i). For a given station we apply a single high-pass frequency,

Table 2

1D Crustal Model Used to Generate the Synthetic Seismograms

Layer Thickness (km)	V_P(km/sec)	V_S(km/sec)	Density (g/cm3)	Q_P	Q_S
0.6	3.3	1.9	2.0	200	100
1.4	4.5	2.6	2.3	350	175
3.0	5.5	3.18	2.5	500	250
25.0	6.5	3.75	2.9	600	300
Mantle	8.1	4.68	3.3	1000	500

V_P, V_S, and Q_P, Q_S are the *P*- and *S*-wave velocities and quality factors, respectively.

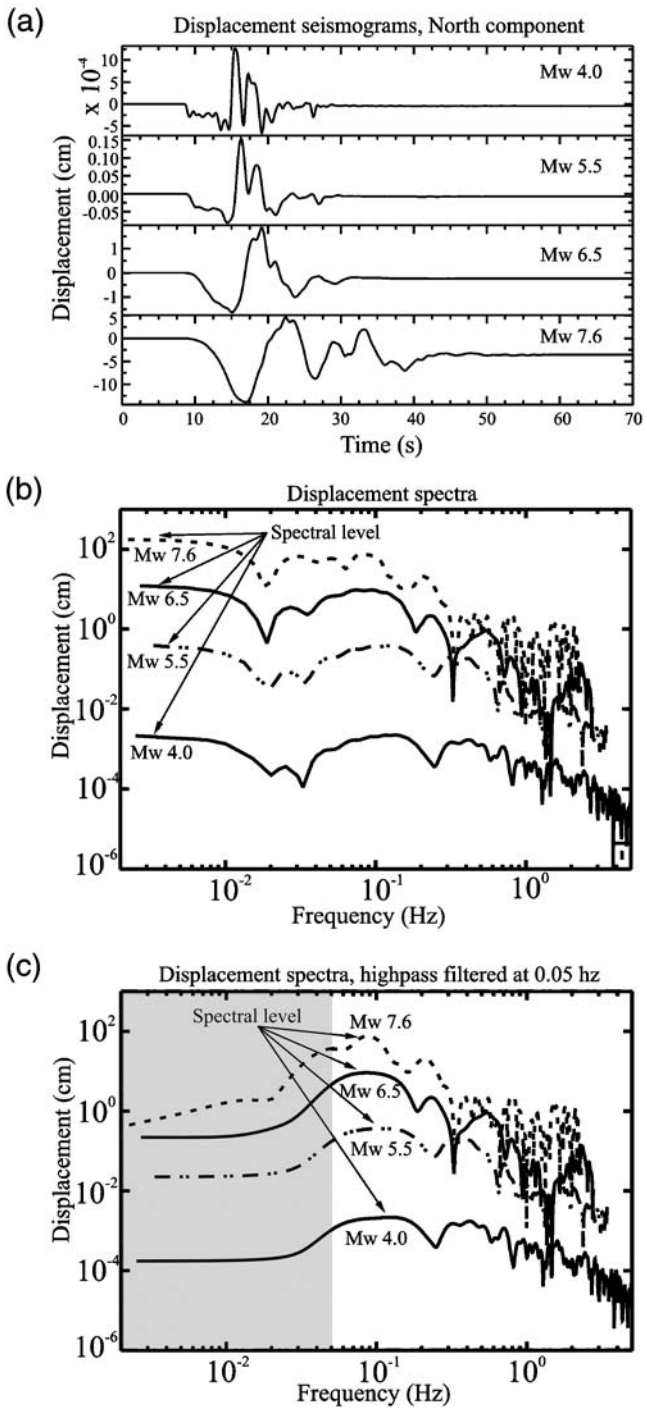

Figure 3. (a) Synthetic displacement seismograms (north component) computed with four different finite dimension source models sized with moment magnitude 4.0, 5.5, 6.5, and 7.6. Focal mechanism (strike/dip/rake) and epicentral distance are (0/45/90) and 52 km, respectively. (b) and (c) Displacement spectra of the same synthetic seismograms, unfiltered (b) and high-pass filtered at 0.05 Hz (c). Computed for a time window ending 80 sec after origin time. The spectral level, corresponding to the highest value of the spectrum at low frequency, is indicated for each magnitude. In part (c) the filtered domain is gray shaded.

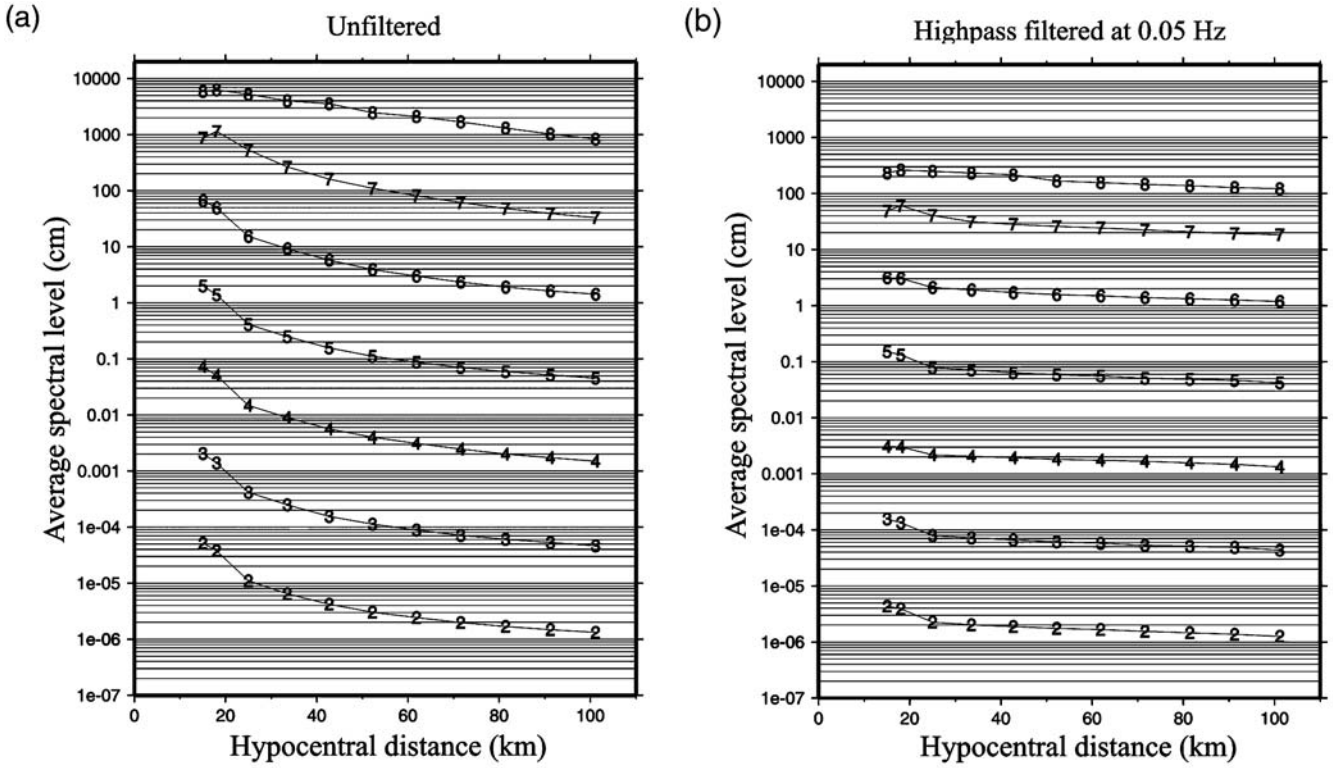

Figure 4. Average spectral level as a function of hypocentral distance and moment magnitude for synthetic displacement seismograms (a) unfiltered and (b) high-pass filtered at 0.05 Hz. The spectral level (highest value on the displacement spectra) is averaged over the three components of the seismograms and over the six different focal mechanisms shown in Figure 2. Labels on the curves indicate moment magnitude (2–8). Computed for a time window ending 80 sec after origin time.

selected as the highest value among the high-pass frequencies found for the three components.

We process successively the different stations that recorded the earthquake. A minimum requisite for a given window to be used is that it should include the first *P*-wave onset and the next three seconds. For an automated selection of the optimal high-pass filtering frequency from the curvature of the initial part of the spectrum, the window should include the *S*-wave onset and the next 20 sec of signal. In the case of a window length shorter than the arrival time of *S* wave +20 sec, the high-pass frequency is fixed in a conservative way to 0.25 Hz.

We integrate twice the acceleration records, apply the selected high-pass filters, and compute the displacement spectra. We retrieve the spectral level as the maximum amplitude of the low-frequency part of the displacement spectrum and compute the average spectral level over the three components of the seismograms. These average values can then be compared with those computed for the synthetic seismograms.

Computing of M_w

We compute the moment magnitude M_w for the different time windows defined in the previous section: 5, 10, 20, 30, 40, 50, 60, 70, and 80 sec after origin time. For each station we select the prestored table of synthetic data corresponding to the same time window and high-pass frequency used to process the observed seismograms. Each table contains the average synthetic spectral levels as a function of magnitude for different predetermined hypocentral distances (Fig. 4). For each station the moment magnitude corresponding to the observed spectral level and to the actual hypocentral distance is found by interpolating in the table values. Figure 6 illustrates the process with station CHY080, which recorded the Chi-Chi earthquake. Interpolation is linear for distance and logarithmic for spectral level.

For each time window M_w is determined as the weighted average of the M_w computed for the individual stations. Considering that the spectral level is better defined and more representative of the actual seismic moment when the low frequencies are better preserved, weight is chosen as the inverse of the high-pass frequency. If more than three stations are available a standard deviation is computed. When the low frequencies are too strongly filtered out a saturation of spectral levels occurs for large magnitudes, a phenomenon that can be deduced by comparing Figure 4a and 4b. Accordingly, we had to define some thresholds for magnitude as a function of the high-pass frequency. Moment magnitude M_w is limited to values 7.0, 7.3, and 7.6 for high-pass frequencies larger than 0.3, 0.1, and 0.08, respectively. Stations for which the magnitude is limited in such a way are down-weighted using a coefficient of one-fifth. The maximum

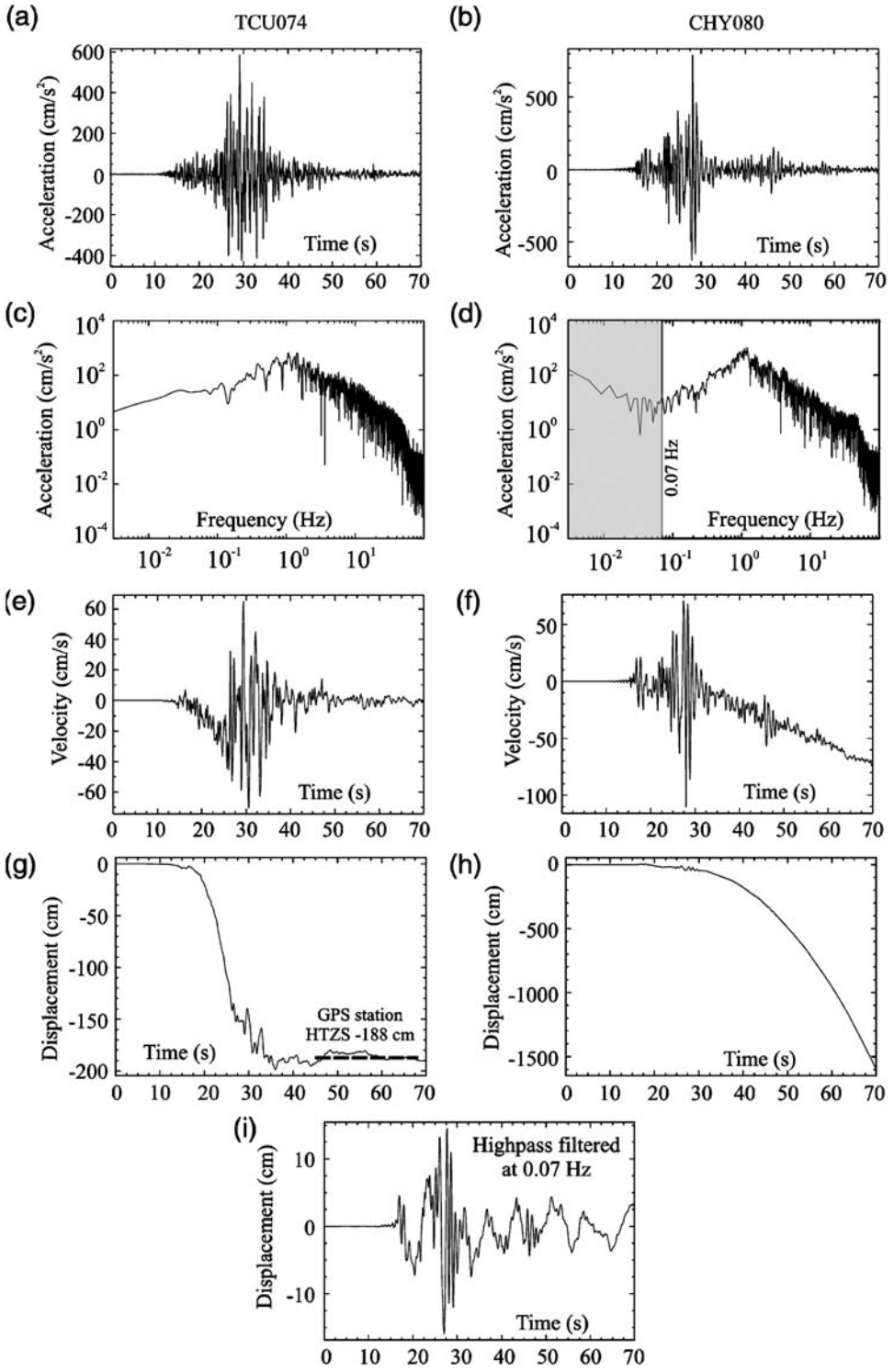

Figure 5. Determination of the high-pass frequency from the acceleration spectra. Illustration for two strong-motion records of the 1999 Chi-Chi earthquake (M_w 7.6, Taiwan). East component of stations TCU074 and CHY080 in the left and right columns, respectively. (a) and (b) Acceleration records. (c) and (d) Acceleration spectra. Note the continuous rise at low frequency for station TCU074 (c) and the initial decay for CHY080 (d), shown in the gray shaded area below 0.07 Hz, resulting in a strong curvature of the low-frequency part of the spectrum. (e) and (f) Velocity seismograms integrated from (a) and (b). A clear linear trend in velocity is observed for station CHY080 (f), implying a baseline shift in acceleration. (g) and (h) displacement seismograms integrated from (e) and (f). For TCU074 (g), a static displacement is found in agreement with nearby Global Positioning System station HTZS (188 cm of displacement toward the west). An unreasonable displacement above 15 m is observed for station CHY080 (h), resulting from the uncorrected baseline shift in acceleration. (i) displacement seismogram for station CHY080 high-pass filtered at 0.07 Hz. Stations TCU074 and CHY080 are located at 20 km and 33 km from the epicenter, respectively.

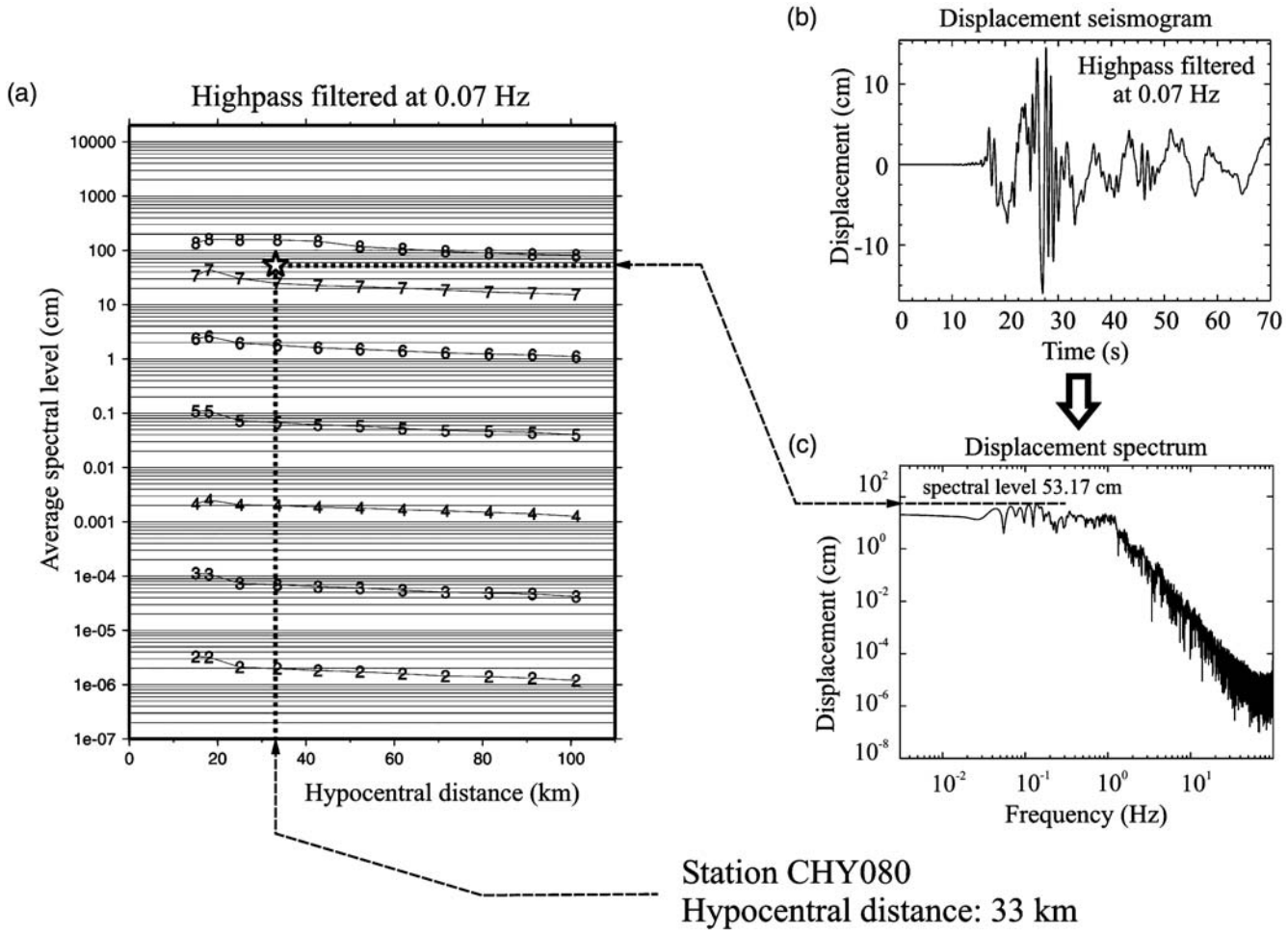

Figure 6. Scheme illustrating the principle of moment magnitude determination. (a) Graphical representation of a table of precomputed values of average spectral level as a function of magnitude and hypocentral distance, for synthetic displacement seismograms high-pass filtered at 0.07 Hz. Labels on the curves indicate moment magnitude. (b) Strong-motion record integrated to displacement and high-pass filtered at 0.07 Hz to remove the baseline shift artifacts. (c) Displacement spectrum obtained from the fast Fourier transform of (b). The spectral level is retrieved from the spectrum. The moment magnitude corresponding to the spectral level (53.17 cm) and to the hypocentral distance (33 km) is obtained by interpolation within the table, as shown by the dashed lines. The point representing the moment magnitude calculated from this record is represented by the white star in (a). In our procedure the spectral levels of the three components of a strong-motion station are averaged. In this figure only the east component of station CHY080 is shown for the sake of simplicity, whereas in reality we average the values over the three components. With this component the magnitude obtained is M_w 7.3.

magnitude that can be determined from the prestored tables is eight. We will draw the average moment magnitude and standard deviation as a function of the time window. We will also show the minimum and maximum M_w computed from individual stations. We select the average magnitude computed with the 80 sec time window as the earthquake moment magnitude.

Validation with Reference Earthquakes

We tested the method on 22 earthquakes for which both digital strong-motion records and a reference moment magnitude were available to us (Table 1). Reference moment magnitude is obtained from various sources depending on availability, such as the GCMT (see Data and Resources section), regional moment tensor solutions, or specific published source inversions. All but five of the earthquakes are shallow continental events (hypocentral depth < 18 km). The remaining five events are subduction related earthquakes with a slightly deeper source (hypocentral depth 36–49 km): Tocopilla (Chile), Miyagi–Oki (Japan), Pingtung 1 and 2 (Taiwan), and Lesser Antilles 3. Nine of the selected events occurred in France (metropolitan area and Lesser Antilles) and were recorded by the French accelerometric network Réseau accélérométrique permanent (RAP, see Data and Resources section). To expand the dataset and incorporate earthquakes of larger magnitude we included events from Turkey (Izmit, Duzce), Algeria (Boumerdes), California (Anza, Parkfield), Japan (Tottori, Miyagi-Oki), Taiwan (Chi-Chi, Chengkung, Taitung, Pingtung), and Chile (Tocopilla). The overall range for M_w is 3.9 to 7.7. We ob-

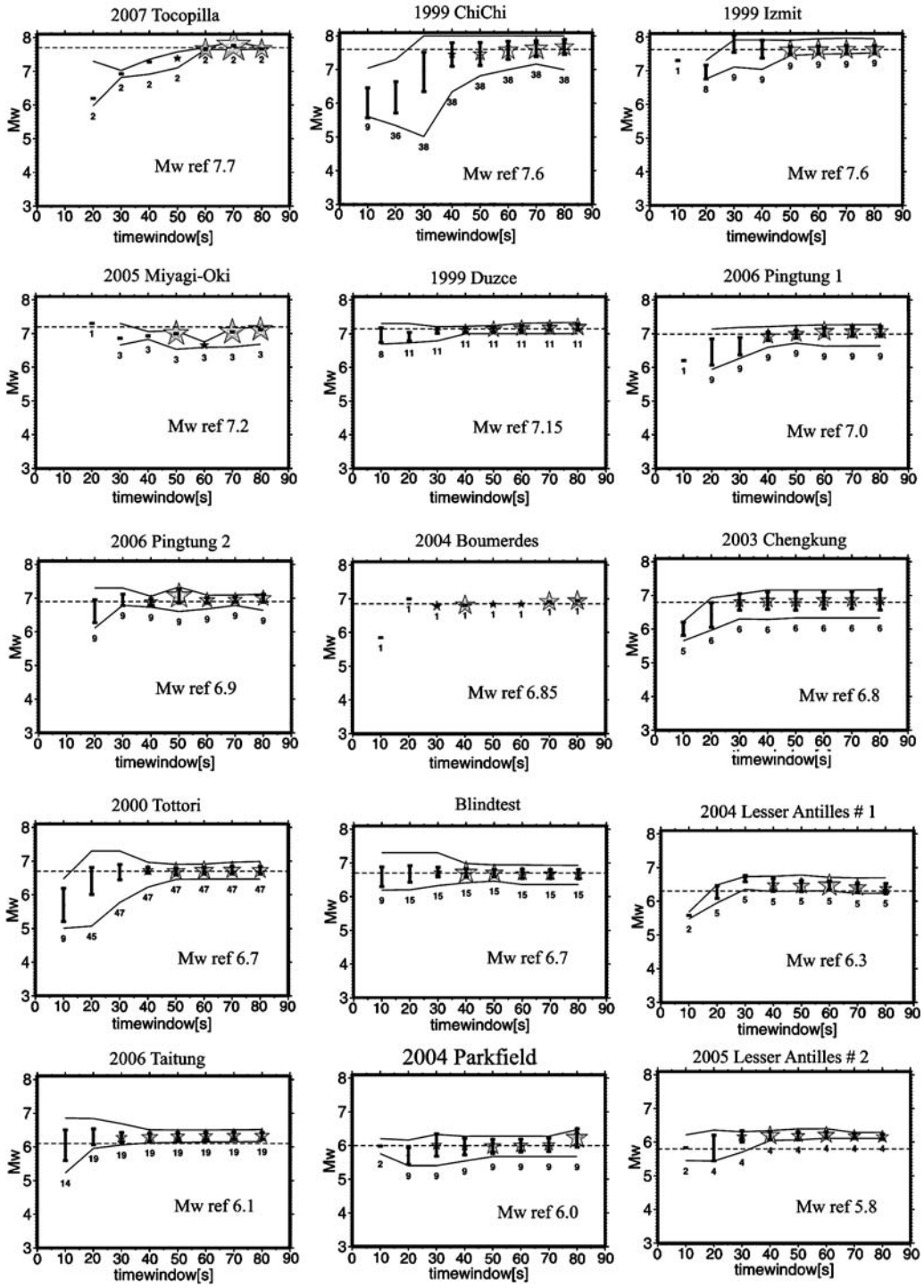

Figure 7. Graphs showing the evolution of computed M_w as a function of time measured from the earthquake origin time ($T = 0$) for various events ranging from M_w 3.9 to 7.7 (Table 1). M_w is obtained by averaging the magnitude values among the different stations that contribute at least 3 sec of seismic signal in the selected time window. A weight is attributed to each individual station depending on the high-pass filtering used (see text). The average M_w is represented by an open star whose size is proportional to the sum of weights. Larger stars are expected to provide better estimates, but size is a relative measure of weight for a given event and cannot be compared from one event to the other. If more than three stations are used, error bars are drawn corresponding to one standard deviation. Continuous lines indicate the maximum and minimum values of magnitude found among the different stations. The reference moment magnitude is indicated (M_w ref) and shown by a dashed line. The number of stations used is indicated for each time increment. (*Continued*)

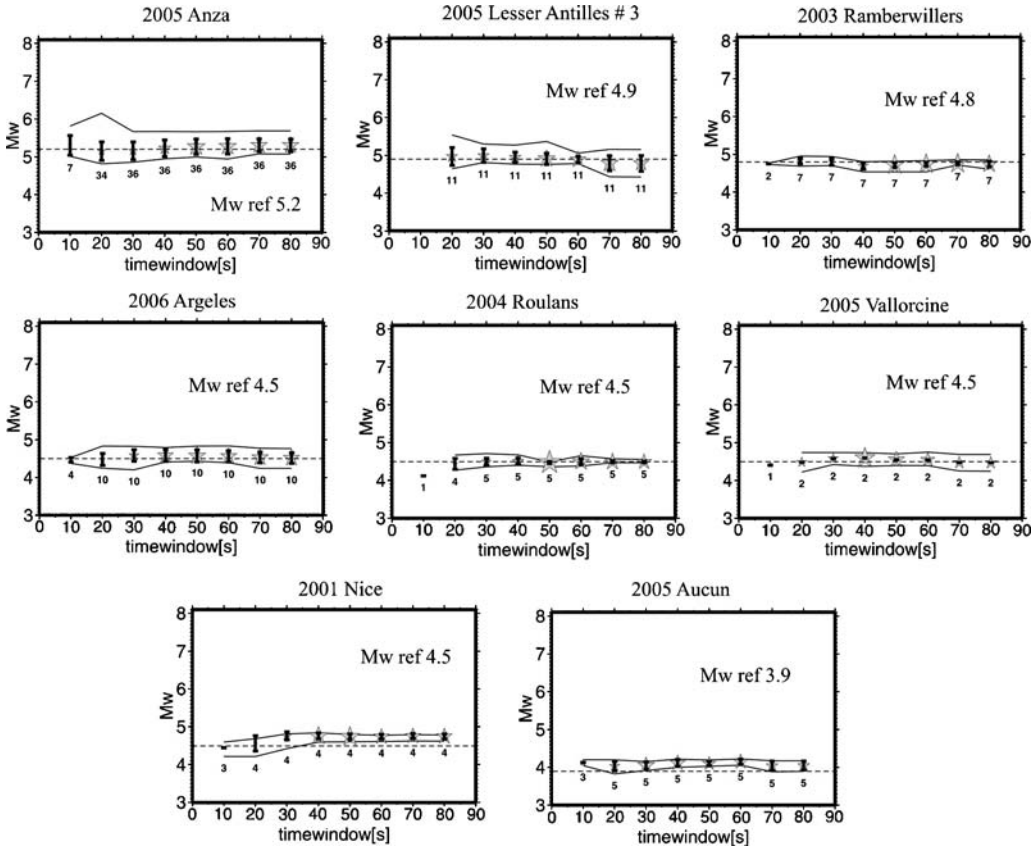

Figure 7. Continued.

tained the digital strong-motion records from the sources described in Table 1 for stations located less than 100 km from the epicenter. The number of stations per event is highly variable, from a single one for Boumerdes to 47 for Tottori. The dataset probably include a great variety of soil conditions, which are not analyzed in this study.

We also made a test with the synthetic data provided by the project SPICE (seismic wave propagation and imaging in complex media: a European network) for blind tests on earthquake source inversion (Mai *et al.*, 2007). These synthetic data are generated with the same fault geometry, station distribution, and moment magnitude as the Tottori earthquake, but with a different slip distribution (blind test model 1, see Data and Resources section).

Results are presented in Figure 7. Moment magnitude tends to stabilize around the reference value for time windows larger than 30–40 sec. In the dataset no station was close enough to the hypocenter to provide a magnitude estimate with the 5 sec time window. For large earthquakes an underestimation of the moment magnitude is often observed for the shortest time windows. This underestimation has essentially two causes. First is the difference in slip distribution between the real and synthetic ruptures. The synthetic seismograms are computed assuming that slip is constant over the rupture plane. In cases where the actual slip distribution is characterized by low slip in the hypocentral area, the method is expected to deliver an underestimated value of M_w for the shortest time windows. Signals in these windows correspond to the waves emitted in the vicinity of the hypocenter. Exemplary cases are the Chi-Chi and Tottori earthquakes whose slip distributions exhibit a small relative amount of slip in the hypocentral area (Ma *et al.*, 2001; Iwata and Sekiguchi, 2002; Ji *et al.*, 2003; Semmane *et al.*, 2005). The second cause of underestimation is related to the high-pass filtering, which is generally set to 0.25 Hz for short time windows. As a result the low frequencies representing the actual earthquake size are partially filtered out, making the characterization of large events more difficult. The fact that short time windows may not include the entire signal from the rupture process should not be a general cause of underestimation of M_w because the synthetic signals are also truncated in the same way. However, because synthetics are computed assuming constant slip along the whole rupture, an underestimation of M_w is expected in cases where slip in the initial part of the real rupture is significantly smaller than the average slip of the earthquake.

Comparison between M_w computed with our method and reference M_w can be found in Figures 7 and 8. The average deviation between our M_w and the reference one is $+0.07$, meaning that on average our moment magnitude is slightly overestimated. The standard deviation between the two M_w is 0.11. The largest deviations are found for

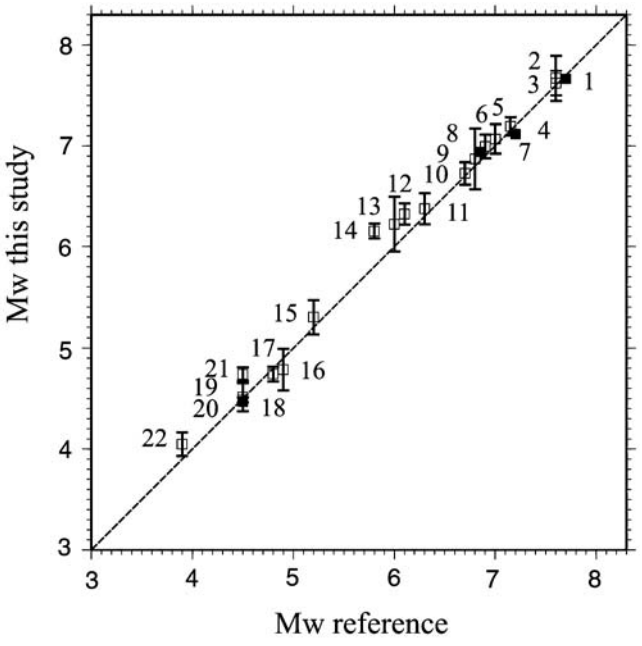

Figure 8. M_w determined in this study versus reference M_w. The values of M_w determined in this study are indicated by open squares with error bars, or black squares without error bars when less than three stations are available. Error bars correspond to one standard deviation. The oblique straight line of slope unity corresponds to identity. Numbers indicate event numbers (Table 1).

the 2005 Saintes (Lesser Antilles 2) event (+0.36) and the 2006 Taitung (Taiwan) earthquake (+0.22).

Discussion and Conclusion

The MWSYNTH method developed in this study provides an overall correct recovery of M_w over a wide range of magnitudes (3.9 to 7.7). These results could be obtained using a time window ending 80 sec after earthquake origin time and with an automated determination of the optimal high-pass frequency.

Some degree of arbitrariness can be found in the choices that were made in the initial step for computing the synthetic seismograms. It essentially concerns the definition of the six different focal mechanisms, the azimuth of the receiver station, the depth of the hypocenter in the fault models, the rupture propagation, and the 1D crustal model.

Focal mechanism, fault orientation, and station azimuth are related in the sense that they define the geometrical relation between the receiver and the rupture plane. The synthetic spectral data account for an average distance to the rupture plane, averaged over the six fault orientations and assuming bilateral ruptures (the hypocenter is systematically located at the center of the rupture plane). In the case of a real unilateral rupture, a station located in the anti directive direction will indeed be located farther from the rupture plane than assumed by the synthetic data. This antidirective station will underestimate M_w. On the other hand, a station located near the actual rupture plane or in the directivity direction will overestimate M_w. We observed this effect with the Chi-Chi earthquake data, which propagated almost unilaterally towards the north. Stations located south of the hypocenter provided the lowest estimates of M_w, the largest values being obtained with stations located more to the north near the fault trace where large slip occurred. However, averaging the effects of the six fault orientations and faulting behaviors considered here (Fig. 2a) with stations distributed in various azimuths around the epicenter should reduces this kind of bias.

We performed a series of sensitivity tests to assess the robustness of the method, varying the model parameters used to compute the synthetic data: focal mechanisms, rupture propagation on the fault plane, hypocenter depth, station azimuth, and velocity model. The results are summarized in Table 3. The tests were carried out for three events spanning the magnitude range of the study (Izmit M_w 7.6; Chengkung M_w 6.8; Argeles M_w 4.5; see Table 1). These tests suggest that M_w is not highly sensitive with respect to the model parameters. The highest deviations are observed when varying the crustal model (Table 3). We note, however, that outlier values of M_w such as the low magnitudes obtained for the Izmit and Argeles events (7.35 and 4.39, respectively) are produced by a crustal model (model Thin platform of CRUST2.0) whose sedimentary layers are much thicker (6 km) than expected in the earthquake areas. Such a crustal model enhances the synthetic spectral levels and in comparison the spectral levels of the real records will be smaller, leading to the underestimation of M_w. On the other hand, we verified that the use of a crustal model including softer sedimentary layers than in the model of Table 2 can reduce the overestimation of M_w for the 2005 Saintes (Lesser Antilles 2) by at least 0.2. A waveform modeling of events in the Saintes area confirmed that such soft sedimentary layers are required (Delouis *et al.*, 2007). This analysis suggests that the performance of the method could be improved by using a velocity model adapted to each study area, something which was beyond the scope of the present study. When targeting a specific network additional improvement could be obtained by taking into account the soil conditions, either by selecting stations located on hard rock or by incorporating site correction functions in the spectral analysis for soft soil sites.

The choice of a frequency of 0.25 Hz for high-pass filtering the records for the shortest time windows is relatively conservative and partially responsible of an underestimation of M_w. However, the choice of a lower frequency would increase the risk of producing biased spectral levels due to incorrect removal of the baseline shift effect. This problem does not affect longer time windows ($>$ 30–40 sec), for which an optimal high-pass cutoff frequency is automatically determined.

The MWSYNTH method can be implemented for automated near real-time determination of M_w. A robust value of M_w may be obtained within about 100 sec after origin time (recording + computing time) with six to ten stations. The

Table 3
Sensitivity Test*

	1999 Izmit	2003 Chengkung	2006 Argeles
M_w reference	7.6	6.8	4.5
M_w with parameters described in The MWSYNTH Method section†	7.62	6.87	4.52
M_w with a different set of focal mechanisms‡	7.56	6.83	4.50
M_w with an uncentered rupture§	7.54	7.00	4.52
M_w with hypocentral depth 8 km‖	7.78	6.90	4.47
M_w with hypocentral depth 25 km#	7.53	6.91	4.61
M_w with test of 18 station Azimuths**	Minimum: 7.57, Maximum: 7.72	Minimum: 6.85, Maximum: 6.96	Minimum: 4.51, Maximum: 4.55
M_w with test of 233 crustal models††	Minimum: 7.35, Max: 7.64	Minimum: 6.85, Maximum: 7.04	Minimum: 4.39, Maximum: 4.69

*Variation of M_w computed for three selected events when the parameters used to generate the synthetic spectral data are modified. The three events, 1999 Izmit, 2003 Chengkung, and 2006 Argeles, are referenced in Table 1.

†Model parameters used throughout this study and described in The MWSYNTH Method section.

‡The six focal mechanisms described in The MWSYNTH Method section are changed to (strike/dip/rake = 20/90/30, 70/70/ − 20, 0/45/ − 90, 120/55/45, 45/45/ − 90, 155/65/ − 120).

§The hypocenter in the fault models is changed. It is shifted with respect to the fault center, by $L/2.5$ in the antistrike direction and $W/2.5$ in the dip direction, where L and W are the rupture model length and width respectively, in km.

‖The depth of the hypocenter of the synthetic fault models is changed to 8 km.

#The depth of the hypocenter of the synthetic fault models is changed to 25 km.

**The station azimuth is varied from 0 to 340 with an increment of 20 degrees.

††Synthetic spectral data are computed using 233 different crustal models issued from the CRUST2.0 global crustal model at 2×2 degrees by Laske, Masters, and Reif (see the Data and Resources section for additional information).

For all tests, parameters not specifically described as changed are as described in The MWSYNTH Method section. When more than one magnitude is computed, the minimal and maximal values found are indicated.

time delay may be reduced by using shorter time windows, but in that case an underestimation of M_w may occur for large ($M > 6$) earthquakes.

A delay of one to two minutes may be well adapted for most regional tsunami warning systems. On the other hand, our magnitude determination may not be fast enough in cases where early seismic warning is needed to trigger automated actions for alert target areas located short distances from the recording stations. In those cases approaches based on the deterministic characteristics of the first few seconds of the *P* waves (e.g., Allen and Kanamori, 2003; Wu and Zhao, 2006; Zollo *et al.*, 2006; Wu and Kanamori, 2008) can give the first magnitude estimate, with our method providing the updated moment magnitude some tens of seconds later. An updated magnitude is needed to confirm the first alert and to manage emergency actions. It is also required to perform more advanced seismological analyses, such as fast source inversions and computation of reliable shake maps.

Data and Resources

Earthquake data (location, reference moment magnitude, strong-motion records) were obtained either from published studies (see reference list) or from diverse institutions whose acronyms are now described: BCSF (Bureau Central Sismologique Français, http://www.seisme.prd.fr/, last accessed December 2008); CGS (Centre National de recherche Appliquée en Génie Parasismique, Algeria, http://www.cgs-dz.org/, last accessed December 2008); CISN (California Integrated Seismic Network, http://www.cisn.org/, last accessed December 2008); COSMOS (virtual data center, consortium of organizations for strong-motion observation system, http://db.cosmos-eq.org/scripts/earthquakes.plx, last accessed December 2008); CWB (Central Weather Bureau, Taiwan, http://www.cwb.gov.tw/V6e/index.htm last accessed December 2008); ESD (European strong-motion database, Ambraseys *et al.*, 2002, http://www.isesd.cv.ic.ac.uk/ESD/frameset.htm, last accessed December 2008); GCMT (Global Centroid Moment Tensor catalog, www.globalcmt.org/CMTsearch.html, last accessed December 2008); GéoAzur, University of Nice—Sophia Antipolis, France, http://www-geoazur.unice.fr/, last accessed December 2008); K-NET (Kyoshin Network, accelerometric data, Japan, http://www.k-net.bosai.go.jp/, last accessed December 2008); IGN (Istituto Geográfico National, Spain, http://www.ign.es/ign/es/IGN/home.jsp, last accessed December 2008); MEDNET–INGV EMRCMT: Istituto Nazionale di Geofisica e Vulcanologia, European—Mediteranean Catalog of Centroid Moment Tensor Solutions, Italy, http://www.bo.ingv.it/RCMT/searchRCMT.html, last accessed December 2008); JMA (Japan Meteorological Agency, http://www.jma.go.jp/jma/indexe.html, last accessed December 2008); NIED (National Research Institute for Earth Science and Disaster Prevention, http://www.bosai.go.jp/e/index.html, last accessed December 2008); OMP (Observatoire Midi Pyrénées, http://www.obs-mip.fr/omp/, last accessed December 2008); RAP (Réseau accélérométrique permanent, http://www-

rap.obs.ujf-grenoble.fr/, last accessed December 2008); RAGIC (joint accelerometric network of the Geophysics and Civil Engineering departments of the University of Chile, www.cec.uchile.cl/~ragic/ragic.htm, last accessed December 2008); RéNaSS (Réseau National de Surveillance Sismique, France, http://renass.u-strasbg.fr/, last accessed December 2008); and SED/ETHZ (Swiss Seismological Service, Swiss Federal Institute of Technology in Zurich, Switzerland, http://www.seismo.ethz.ch/, last accessed July 2008). For more information on the SPICE blind test model 1 see http://www.seismo.ethz.ch/staff/martin/BlindTest.html (last accessed April 2009).

Some figures were partly made using the Generic Mapping Tools package by Wessel and Smith (www.soest.hawaii.edu/gmt, last accessed December 2008)

Seismic data processing was partly done using the Seismic Analysis Code package by Peter Goldstein (http://www.iris.edu/software/sac/sac.request.htm, last accessed December 2008)

Additional information on the CRUST2.0 global crustal model by Laske, Masters, and Reif referenced in Table 3 is available at http://mahi.ucsd.edu/~gabi/rem.dir/crust/crust2.html (last accessed April 2009).

Acknowledgments

This work was carried out in the framework and under the support of the European Community-Seismic Early Warning for Europe project. It was also supported by the French Ministère de l'Ecologie du Développement et de l'Aménagement Durables through the RAP program. We are grateful to the two anonymous reviewers who helped to improve the manuscript.

References

Aki, K., and P. G. Richards (1980). Quantitative Seismology, Vol. **1**, W. H. Freeman and Co., San Francisco, 512 pp.

Allen, R. M., and H. Kanamori (2003). The potential for earthquake early warning southern California, *Science* **300,** 786–789.

Ambraseys, N., P. Smit, R. Sigbjornsson, P. Suhadolc, and B. Margaris (2002). *Internet Site for European Strong-Motion Data*, http://www.isesd.cv.ic.ac.uk/ESD/frameset.htm, European Commission, Research-Directorate General, Environment and Climate Programme (last accessed April 2009).

Ayhan, M. E., R. Bürgmann, S. McClusky, O. Lenk, B. Aktug, E. Herece, and R. E. Reilinger (2001). Kinematics of the M_w 7.2 12 November 1999 Düzce, Turkey earthquake, *Geophys. Res. Lett.* **28,** no. 2, 367–370.

Bertil, D., S. Bazin, D. Mallarino, and F. Beauducel (2005). Localisation des principales répliques du séisme des Saintes du 21 Novembre (2004), Centre de Données Sismologiques des Antilles (CDSA), 15 Avril 2005.

Boore, D. M. (2001). Effect of baseline corrections on displacement and response spectra for several recordings of the 1999 Chi-Chi, Taiwan earthquake, *Bull. Seismol. Soc. Am.* **91,** 1199–1211.

Bouchon, M. (1981). A simple method to calculate Green's functions for elastic layered media, *Bull. Seismol. Soc. Am.* **71,** no. 4, 959–971.

Brune, J. N. (1970). Tectonic stress and the spectra of seismic shear waves of earthquakes, *J. Geophys. Res.* **75,** no. 26, 4997–5009.

Brune, J. N. (1971). Correction, *J. Geophys. Res.* **76,** no. 20, 5002.

Bürgmann, R., M. E. Ayhan, E. J. Fielding, T. J. Wright, S. McClusky, B. Aktug, C. Demir, O. Lenk, and A. Türkezer (2002). Deformation during the 12 November 1999 Düzce, Turkey earthquake from GPS and InSAR data, *Bull. Seismol. Soc. Am.* **92,** no. 1, 161–171.

Chang, C. H., Y. M. Wu, T. C. Shin, and C. Y. Wang (2000). Relocation of the 1999 Chi-Chi earthquake in Taiwan, *TAO* Vol. **11,** no. 3, 581–590.

Delouis, B., D. Giardini, P. Lundgren, and J. Salichon (2002). Joint inversion of InSAR, GPS, teleseismic, and strong-motion data for the spatial and temporal distribution of earthquake slip: Application to the 1999 Izmit mainshock, *Bull. Seismol. Soc. Am.* **92,** 278–299.

Delouis, B., M. Pardo, D. Legrand, and T. Monfret (2009). The M_w 7.7 Tocopilla earthquake of 14 November 2007 at the southern edge of the northern Chile seismic Gap: Rupture in the deep part of the coupled plate interface, *Bull. Seismol. Soc. Am.* **99,** 87–94.

Delouis, B., M. Vallée, and V. Cruz-Atienza (2007). The M_w 6.3 Saintes earthquake (West Indies): Source kinematics determination and uncertainties in a poorly known crustal structure, *Geophysical Research Abstracts*, Vol. **9**, European Geosciences Union, 10050, SRef-ID: 16077962/gra/EGU2007-A-10050.

Delouis, B., M. Vallée, M. Meghraoui, E. Calais, S. Maouche, K. Lammali, A. Mahsas, P. Briole, F. Benhamouda, and K. Yelles (2004). Slip distribution of the 2003 Boumerdes Zemmouri earthquake, Algeria, from teleseismic, GPS, and coastal uplift data, *Geophys. Res. Lett.* **31,** L18607, doi 10.1029/2004GL020687.

Iwan, W. D., M. A. Moser, and C. Y. Peng (1985). Some observations on strong-motion earthquake measurement using a digital accelerograph, *Bull. Seismol. Soc. Am.* **75,** 1225–1246.

Iwata, T., and H. Sekiguchi (2002). Source process and near-source ground motion during the 2000 Tottori-ken Seibu earthquake, Presented at the *11th Japan Earthquake Engineering Symposium*, Tokyo, Japan.

Ji, C., D. V. Helmberger, D. J. Wald, and K. F. Ma (2003). Slip history and dynamic implications of the 1999 Chi-Chi, Taiwan earthquake, *J. Geophys. Res.* **108,** no. B9, 2412, doi 10.1029/2002JB001764.

Kanamori, H. (1977). The energy release in great earthquakes, *J. Geophys. Res.* **82,** 2981–2987.

Liu, P., S. Custódio, and R. J. Archuleta (2006). Kinematic inversion of the 2004 *M* 6.0 Parkfield earthquake including an approximation to site effects, *Bull. Seismol. Soc. Am.* **96,** no. 4B, S143–S158, doi 10.1785/0120050826.

Ma, K. F., J. Mori, S. J. Lee, and S. B. Yu (2001). Spatial and temporal slip distribution of the Chi-Chi, Taiwan earthquake from strong motion, teleseismic, and GPS data, *Bull. Seismol. Soc. Am.* **91,** 1069–1087.

Mai, P. M., D. Monelli, G. Festa, C. Francois-Holden, J. Burjanek, S. Di Carli, B. Delouis, J. Zahradnik, J. P. Ampuero, and R. Madariaga (2007). Source-inversion blindtest: Initial results and further developments, *Geophysical Research Abstracts*, Vol. **9**, European Geosciences Union, 07351, SRef-ID: 1607-7962/gra/EGU2007-A-07351.

Milkereit, C., S. Zünbül, S. Karakisa, Y. Iravul, J. ZschauSABO group, M. Baumbach, H. Grosser, E. Günther, N. Umutlu, T. Kuru, E. Erkul, L. Klinge, M. Ibs von Seht, and A. KarahanTask Force (2000). Preliminary aftershock analysis of the M_w 7.4 Izmit and M_w 7.1 Düzce earthquake in western Turkey, in *The Izmit and Düzce Earthquakes: Preliminary Results*, A. Barka, O. Kozaci, S. Altunel, and E. Akyüz (Editors), Istanbul Technical University, Turkey, 178–187.

Mozziconacci, L., B. Delouis, J. Angelier, J. C. Hu, and B. S. Huang (2008). Slip distribution on a thrust fault at a plate boundary: The 2003 Chengkung earthquake, Taiwan, *Geophys. J. Int.* **177,** no. 2609–623.

Ohmi, S., K. Watanabe, T. Shibutani, N. Hirano, and S. Nakao (2002). The 2000 western Tottori earthquake—seismic activity revealed by the regional seismic networks, *Earth Planets Space* **54,** 819–830.

Reilinger, R. E., S. Ergintav, R. Bürgmann, S. McClusky, O. Lenk, A. Barka, O. Gurkan, L. Hearn, K. L. Feigl, R. Cakmak, B. Aktug, H. Ozener, and M. N. Toksöz (2000). Coseismic and postseismic fault slip for the 17 August 1999 *M* 7.5 Izmit, Turkey earthquake, *Science* **289,** 1519–1524.

Semmane, F., F Cotton, and M. Campillo (2005). The 2000 Tottori earthquake: A shallow earthquake with no surface rupture and slip proper-

ties controlled by depth, *J. Geophys. Res.* **110,** B03306, doi 10.1029/2004JB003194.

Tibi, R., G. Bock, Y. Xia, M. Baumbach, H. Grosser, C. Milkereit, R. Kind, and J. Zschau (2001). Rupture processes of the August 17 Izmit and November 12, 1999 Düzce (Turkey) earthquakes, *Geophys. J. Int.* **144,** F1–F7.

Wells, D. L., and K. J. Coppersmith (1994). New empirical relationships among magnitude, rupture length, rupture width, rupture area, and surface displacement, *Bull Seismol. Soc. Am.* **84,** 974–1002.

Wu, R. S., and A. Ben-Mehahem (1985). The elastodynamic near field, *Geophys. J. R. Astr. Soc.* **81,** 609–621.

Wu, Y.-M., and H. Kanamori (2008). Development of an earthquake early warning system using real-time strong-motion signals, *Sensors* **8,** 1–9.

Wu, Y.-M., and T. L. Teng (2004). Near real-time magnitude determination for large crustal earthquakes, *Tectonophysics* **390,** 205–216.

Wu, Y.-M., and C. F. Wu (2007). Approximate recovery of coseismic deformation from Taiwan strong-motion records, *J. Seismol.* **11,** 159–170.

Wu, Y.-M., and L. Zhao (2006). Magnitude estimation using the first three seconds *P*-wave amplitude in earthquake early warning, *Geophys. Res. Lett.* L16312, doi 10.1029/2006GL026871.

Wu, Y.-M., Y. G. Chen, T. C. Shin, H. Kuochen, C. S. Hou, J. C. Hu, C. H. Chang, C. F. Wu, and T. L. Teng (2006a). Coseismic versus interseismic ground deformations, fault rupture inversion, and segmentation revealed by 2003 M_w 6.8 Chengkung earthquake in eastern Taiwan, *Geophys. Res. Lett.* **33,** L02312, doi 10.1029/2005GL024711.

Wu, Y.-M., Y.-G. Chen, C. H. Chang, L. H. Chung, T. L. Teng, F. T. Wu, and C. F. Wu (2006b). Seismogenic structure in a tectonic suture zone: With new constraints from 2006 M_w 6.1 Taitung earthquake, *Geophys. Res. Lett.* **33,** L22305, doi 10.1029/2006GL027572.

Yagi, Y., and M. Kikuchi (2000). Source rupture process of the Kocaeli, Turkey earthquake of August 17, 1999, obtained by joint inversion of near-field data and teleseismic data, *Geophys. Res. Lett.* **27,** 1969–1972.

Zollo, A., M. Lancieri, and S. Nielsen (2006). Earthquake magnitude estimation from peak amplitudes of very early seismic signals on strong-motion records, *Geophys. Res. Lett.* **33,** L23312, doi 10.1029/2006GL027795.

Géosciences Azur
University of Nice-Sophia Antipolis
CNRS, IRD, 250 rue A. Einstein
06560, France
delouis@geoazur.unice.fr
charlety@geoazur.unice.fr
martin.vallee@geoazur.unice.fr

Manuscript received 11 August 2008